ADVANCES IN ATMOSPHERIC SCIENCES, VOL. 26, NO. 1, 2009, 78–86

Synchronization of Radar Observations with Multi-Scale Storm Tracking

YANG Hongping*[1] (杨洪平), Jian ZHANG[2], and Carrie LANGSTON[2]

[1] *Wuhan Institute of Heavy Rain, China Meteorological Administration, Wuhan* 430074

[2] *Cooperative Institute for Mesoscale Meteorological Studies, The University of Oklahoma, and NOAA/OAR National Severe Storms Laboratory, Norman, O.K., U.S.A*

(Received 14 October 2007; revised 4 June 2008)

ABSTRACT

The 3-D radar reflectivity data has become increasingly important for use in data assimilation towards convective scale numerical weather prediction as well as next generation precipitation estimation. Typically, reflectivity data from multiple radars are objectively analyzed and mosaiced onto a regional 3-D Cartesian grid prior to being assimilated into the models. One of the scientific issues associated with the mosaic of multi-radar observations is the synchronization of all the observations. Since radar data is usually rapidly updated (∼every 5–10 min), it is common in current multi-radar mosaic techniques to combine multiple radar' observations within a time window by assuming that the storms are steady within the window. The assumption holds well for slow evolving precipitation systems, but for fast evolving convective storms, this assumption may be violated and the mosaic of radar observations at different times may result in inaccurate storm structure depictions. This study investigates the impact of synchronization on storm structures in multiple radar data analyses using a multi-scale storm tracking algorithm.

Key words: synchronization, radar, multi-scale storm tracking

Citation: Yang, H. P., J. Zhang, and C. Langston, 2009: Synchronization of radar observations with multi-scale storm tracking. *Adv. Atmos. Sci.*, **26**(1), 78–86, doi: 10.1007/s00376-009-0078-0.

1. Introduction

Because of the high spatial and temporal resolutions of radar data, they have been widely used in many meteorological applications such as severe storm monitoring and warnings (e.g., Johnson et al., 1998; Witt et al., 1998; Mitchell et al., 1998; Smith et al., 2004), convective scale numerical weather predictions (NWP)(e.g., Sun and Crook, 1998; Zhang, 1999; Brewster, 2003; Gao et al., 2004; Hu et al., 2006; Sheng et al., 2006), as well as quantitative precipitation estimation (QPE) and forecast (QPF) (e.g., Anagnostou and Krajewski, 1999; Fulton et al., 1998; Liu et al., 2001; Golding, 1998). The National Weather Service (NWS) has implemented the communication infrastructure that facilitates the central collection and distribution of base level data in real time from ∼140 WSR-88D (Weather Surveillance Radar-1988 Doppler) sites to several centralized locations or hubs. End users from government agencies, universities and private industries can access and retrieve the base level data in real-time from the centralized hubs. The United States National Oceanic and Atmospheric Administration's National Severe Storms Laboratory (NSSL), utilizing the communication infrastructure, has instituted a National Mosaic and Quantitative Precipitation Estimation (NMQ) system and research program (Zhang et al., 2004; Seo et al., 2005). The NMQ system takes base level data from all available radars at any given time, performs quality control, and then combines reflectivity observations from individual radars onto a unified 3-D Cartesian grid that covers the contiguous United States (CONUS). One of the scientific issues associated with the mosaic of multi-radar observations is the synchronization of all the observations. The objective of the current study is to evaluate the impact of synchronization on storm structures in multi-radar analyses.

*Corresponding author: YANG Hongping, yhp_2001@hotmail.com

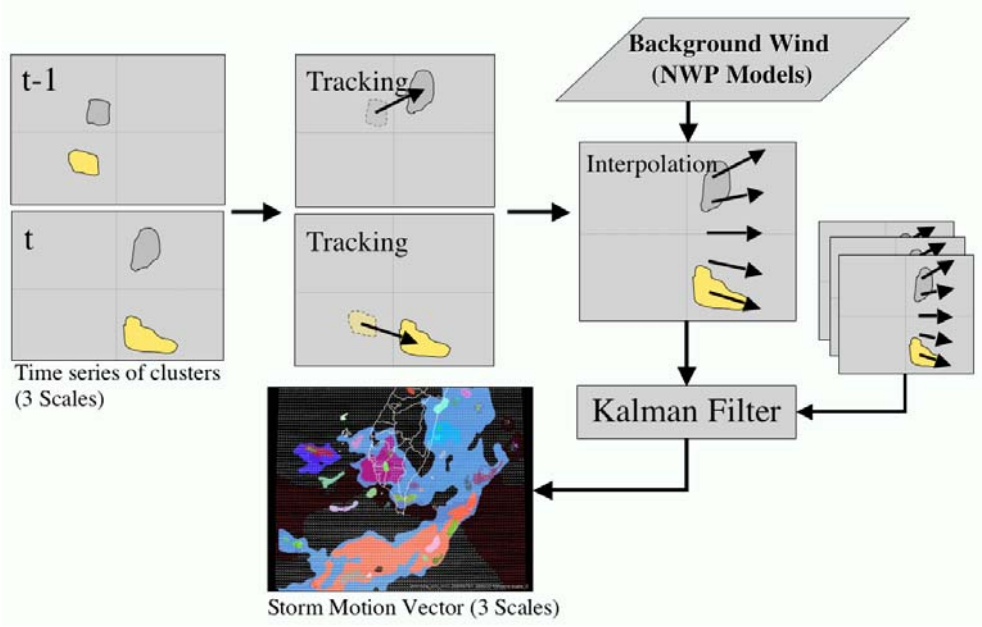

Fig. 1. A flowchart shows the process of storm motion estimation.

Table 1. Operational scan modes used in the WSR-88D network.

VCP	Used For	Number of Elevations	Time to Complete
VCP31	Clear air, Light snow	5	10 min
VCP32	Clear air, Light snow, Large velocity	5	10 min
VCP21	Precipitation	9	5 min
VCP11	Severe storms	14	6 min
VCP12	Severe storms, Rapid update, Higher resol. at low levels	14	4 min
VCP121	Precipitation, Mitigate range/velocity aliasing	9	6 min

The WSR-88D radars operate in six different scan modes, or Volume Coverage Patterns (VCPs). The time that one radar takes to complete a full volume scan is different for each VCP. For example, VCP 11 consists of 14 elevation scans, taking 5 minutes to complete a volume scan, while VCP 12 consists of 15 elevation scans with one volume scan taking 4 minutes to complete (Table 1). Different radars in the network operate in different VCPs depending on the weather in the vicinity of the radars. Further, the volume scans from adjacent radars do not start and end at the same times.

It is common in current multi-radar mosaic techniques (e.g., Zhang et al., 2005) to combine multiple radar' observations within a time window by assuming that storms are steady within the window. Other 3-D mosaic schemes (e.g., Langston et al., 2007) combine multiple radar observations by using weighting functions both in space and in time. For slowly evolving, slowly moving storms, these analysis schemes work quite well. For fast evolving, fast moving precipitation systems, however, neglecting the time differences between different observations may result in inaccurate depictions of the storm structure in the final analysis (Langston et al., 2007). For instance, one small storm cell would be observed by two radars at two different locations if the two radars volume scans were observed at different times. When combining the two volume scans, one storm cell now at a different location will become a larger cell or even two small cells, if the initial cell had moved outside its echo region observed by the other radar. Lakshmanan et al. (2006) showed the impact of multi-radar data synchronization on a squall line event using a storm-tracking scheme developed by Lakshmanan et al. (2003). The results showed reduced smearing and increased hail size estimation after the synchronization. The current study takes it a step further and tries to quantify the impact of the synchronization on radar reflectivity analyses by comparing reflectivity observations from several close-by radars during a squall line event.

The rest of the paper is organized as follows. Section 2 provides a brief description of the storm-tracking algorithm. A set of experiments was carried

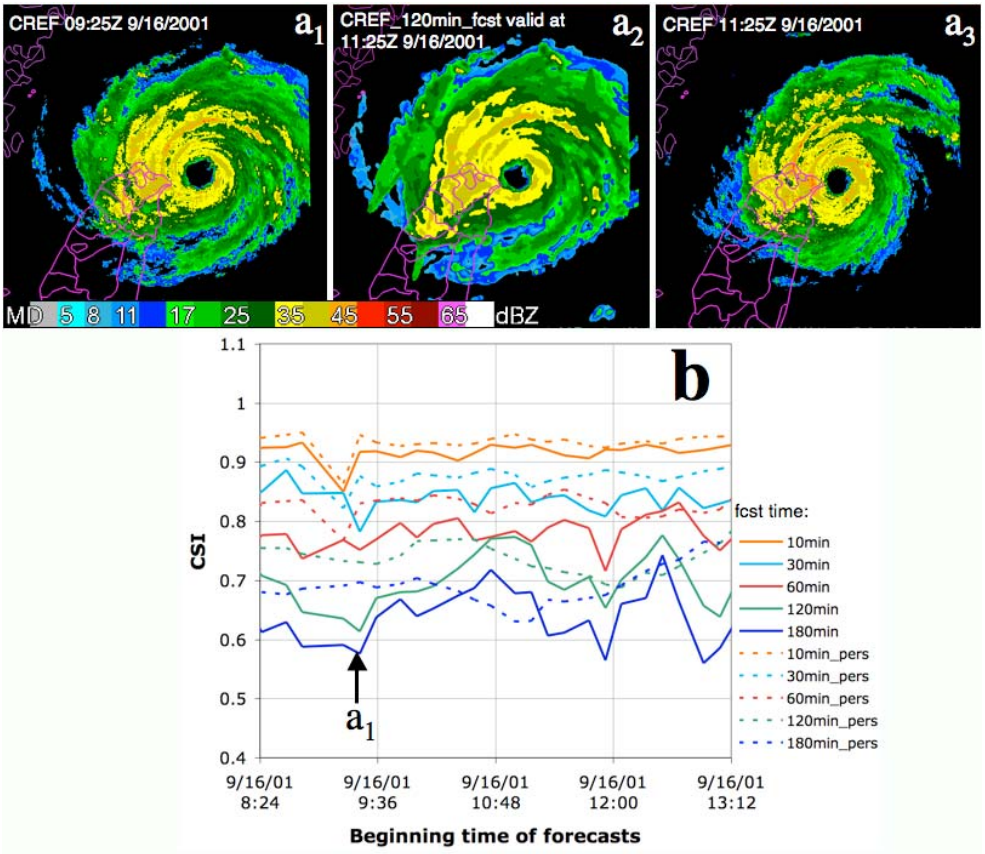

Fig. 2. Observed composite reflectivity fields valid at 0925 (a_1) and 1125 UTC (a_3) of Typhoon Nari and the 120 min forecast of composite reflectivity valid at 1125 UTC (a_2) on 16 September 2001. The CSI scores (b) for multi-scale storm tracking forecasts (solid lines) and for persistence forecasts (dashed lines) of composite reflectivity of 20 dBZ and higher are also shown. The forecast lengths are 10, 30, 60, 120, and 180 min, respectively.

out to evaluate the impact of the synchronization scheme. The experimental design and case study results from a squall line event are presented in section 3 and a summary is provided in section 4.

2. Multi-scale storm tracking

A multi-scale storm-tracking algorithm developed by Lakshmanan et al. (2003) has been adapted for deriving storm motion vector fields used by the synchronization. The algorithm includes the following steps:

(1) Identify individual storm cells at a small scale (pre-specified) based on reflectivity and its spatial gradient fields;

(2) Merge storm cells into larger scale storm entities based on their spatial consistency;

(3) Estimate storm motions, one vector for each storm cell/cluster, by minimizing the difference between the corresponding clusters in consecutive reflectivity images (Fig. 1);

(4) Estimate the growth/decay rate of the storm intensity for each cell/entity;

(5) Analyze/interpolate the storm motion vectors to obtain a gridded motion vector field (Fig. 1);

(6) A Kalman filter is applied to a time series of the motion vector fields to remove random errors in the motion estimates (Fig. 1);

(7) Extrapolate the latest reflectivity observations using motion vectors at different scales into the future to get a forecast. The small-scale motion vectors are used for short-term extrapolations/forecasts and large-scale motion vectors are used for relatively long-term forecasts. The growth/decay factor is also considered in the forecasts.

The multi-scale storm-tracking scheme has been applied to satellites for severe storm applications (Lakshmanan et al., 2003). In the current study, we evaluate it using several precipitation events including 3 typhoon cases and one tornadic supercell case. Figures 2 and 3 show the critical success index (CSI) scores

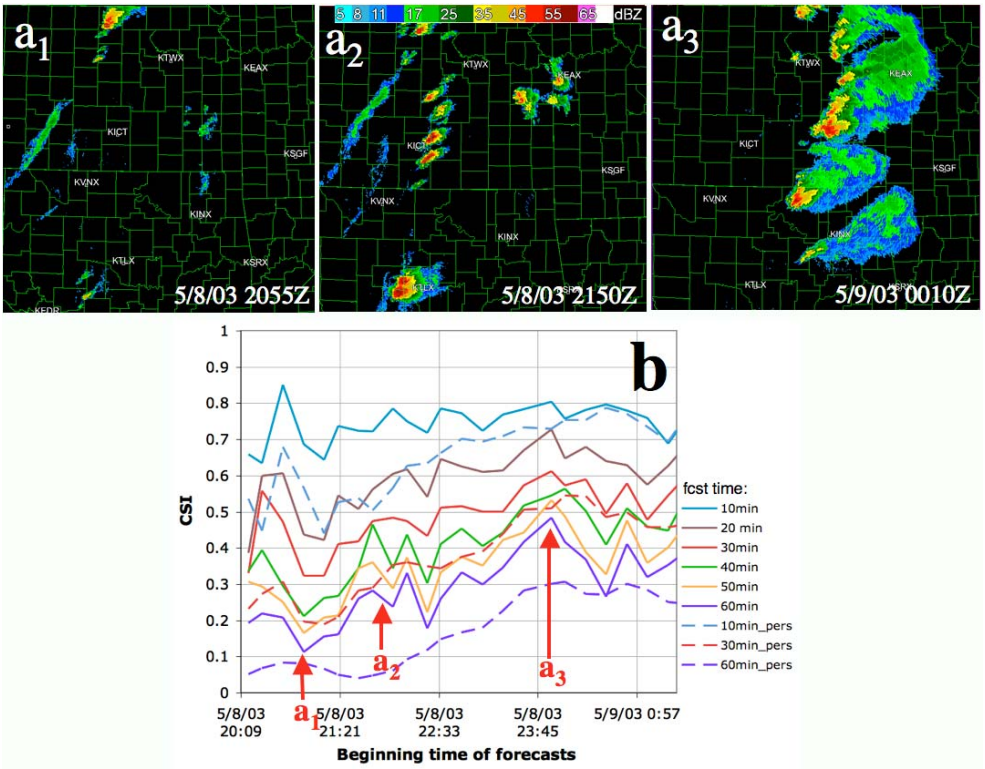

Fig. 3. Composite reflectivity images at (a_1) 2055 UTC, (a_2) 2150 UTC and (a_3) 0010 UTC of the Oklahoma tornado case on 8 May 2003 and (b) the CSI scores for forecasts of composite reflectivity of 20 dBZ and higher. The forecast lengths are 10, 20, 30, 40, 50, and 60 min, respectively. The red arrows indicate three different storm stages as shown in panels a_1, a_2, and a_3, respectively. It is apparent that the poor CSI score (at a_1, panel b) was associated with the initial and fast-growing stage of the storms (panel a_1) while the good CSI (at a_3, panel b) was associated with the mature and well-organized stage of the storms (panel a_3). The CSI for persistent forecasts of 10, 30, and 60 min are shown as the dash line in (b). More discussions can be found in the text.

for reflectivity forecasts of 20 dBZ or higher for one of the typhoon cases and for the tornadic supercell case.

The CSI is defined as

$$\mathrm{CSI} = \frac{X}{X + Y + Z}$$

where X is the number of hits, Y is the number of misses, and Z is the number of false forecasts. The forecasts did quite well for the typhoon case given the relatively slow movement and large area of the precipitation. The CSI scores are higher than 0.6 for most of the forecasts, including the 3-h forecasts (Fig. 2b). However, the slow movement and wide spread precipitation resulted in an even better performance of persistence forecasts than the storm tracking forecast. Figure 2b shows that the CSIs for the persistence forecasts are higher than the storm-tracking forecasts most of the time. Detailed examinations of the forecasts indicated that the poorer performance of the multi-scale tracking scheme was due to the smoothing and smearing in the storm clustering and advecting procedure. The smoothing expanded the precipitation area and caused higher false alarm rates and lower CSIs when the typhoon precipitation area was shrinking with time (e.g., from 0925 to 1125 UTC on 16 September 2001, Figs. 2a_1 and 2a_3). Nevertheless, the storm-tracking correctly forecasted the movement of the typhoon eye (Figs. 2a_2 and 2a_3). When the typhoon precipitation area increased with time (e.g., from 1050 to 1350 UTC, not shown), the storm-tracking forecast performed better than the persistence forecast (Fig. 2b). These results show that the synchronization of radar data may not provide positive impacts for slow moving precipitation systems due to errors in the estimated motion vectors and in the forecast scheme.

For the tornadic supercell case, the forecast performances were mixed. At the initial stage when the storms underwent a fast-growing period (Fig. 3a_1), the CSI scores were relatively low, with a 20 minute

Table 2. List of volume scans of data that were used in the study of synchronization in the 3D Mosaic. Note that the time in the table indicates minutes and seconds after 0600 UTC on 1 June 2005.

Radar	Scan Strategy	Number of Vol. Scans	Time at the Middle of Each Volume Scans
KDYX	VCP11	6	$06'43''$, $11'47''$, $16'52''$, $21'58''$, $27'03''$, $32'09''$
KFWS	VCP11	5	$03'17''$, $08'14''$, $15'57''$, $25'12''$, $29'10''$
KSJT	VCP12	6	$05'08''$, $09'28''$, $13'48''$, $18'06''$, $26'44''$, $31'03''$
KEWX	VCP21	5	$04'47''$, $10'35''$, $16'22''$, $22'11''$, $27'58''$

Table 3. List of the synchronization experiments between the times of the validation grid and testing grid pairs in the experiments. Note that the time indicates the UTC time (rounded to the nearest one) on 1 June 2005 at the middle of the volume scan.

Validation Grid (KDYX)	Test Grid (KFWS)		Test Grid (KEWX)		Test Grid (KSJT)	
Time	Time	Exp. ID	Time	Exp. ID	Time	Exp. ID
0607	0603	KDYX(07)KFWS(03)	0605	KDYX(07)KEWX(05)	0605	KDYX(07)KSJT(05)
0612	0608	KDYX(12)KFWS(08)	0611	KDYX(12)KEWX(11)	0609	KDYX(12)KSJT(09)
0617	0616	KDYX(17)KFWS(16)	0616	KDYX(17)KEWX(16)	0614	KDYX(17)KSJT(14)
0622	0616	KDYX(22)KFWS(16)	0622	KDYX(22)KEWX(22)	0618	KDYX(22)KSJT(18)
0627	0625	KDYX(27)KFWS(25)	0622	KDYX(27)KEWX(22)	0627	KDYX(27)KSJT(27)
0632	0629	KDYX(32)KFWS(29)	0628	KDYX(32)KEWX(28)	0631	KDYX(32)KSJT(31)

forecast CSI below 0.5 (e.g., before 2100 UTC, Fig. 3b). As the storm cells reached certain sizes (Fig. $3a_2$), the CSI scores started to improve rapidly even if the storms were relatively isolated and scattered (e.g., after 2230 UTC, Fig. 3). When the storms became mature and well organized (Fig. $3a_3$), the CSI scores were very good (e.g., after 2330 UTC, Fig. 3) with a 40 minute forecast CSI above 0.5. Overall, the average CSI score was ∼0.5 for the 20 min forecasts (Fig. 3), indicating that the estimated motion vectors were representative of the storm movements within 20 min. The persistence forecast for this case was obviously worse than the storm-tracking forecast (Fig. 3b) because of the fast evolving nature of this tornadic supercell event. Therefore, synchronization of multiple radar observations for applications in these types of events is necessary and justified.

3. Synchronization experiments and evaluation

3.1 *The data*

To quantitatively evaluate the impact of synchronization on radar analysis, detailed experiments were carried out using base level data from four radars (KDYX, KFWS, KEWX, and KSJT) for a squall line event that occurred on 1 June 2005 in central Texas. The radar observations covered a half-hour time period between 0600 to 0630 UTC (see Table 2). Figure 4 shows the composite reflectivity fields from the four radars around 0600 UTC. Table 2 lists all the volume scans from the four radars that are used in the current study.

3.2 *Experimental design*

The experiments were designed as follows:

(1) Each volume scan of reflectivity data was analyzed separately through a common 3-D Cartesian grid (Fig. 4). The valid time of each analysis grid was determined to be the center point between the start and end times of the volume scan.

(2) The KDYX composite reflectivity fields from the 3D analysis grid were used for verification or truthing of the synchronization. Composite reflectivity analyses (with and without advection in time) from the three other radars were compared with the "true" fields from the KDYX radar analysis. A correlation coefficient, ρ, is computed between the "true" composite reflectivity and the testing composite reflectivity analyses. The correlation coefficient is by definition the ratio

$$\rho_{xy} = \frac{\sum_{i=1}^{N}(x_i - \eta_x)(y_i - \eta_y)}{\sqrt{\sum_{i=1}^{N}(x_i - \eta_x)^2}\sqrt{\sum_{i=1}^{N}(y_i - \eta_y)^2}}, \qquad (1)$$

N is the total number of valid composite reflectivity data pairs in the analysis domain. η_x and η_y are the mean of two random variables x (i.e., composite reflectivity from the KDYX reflectivity analysis grid in the current study) and y (i.e., composite reflectivity from any other radar analysis grid before or after synchronization). The means are calculated by:

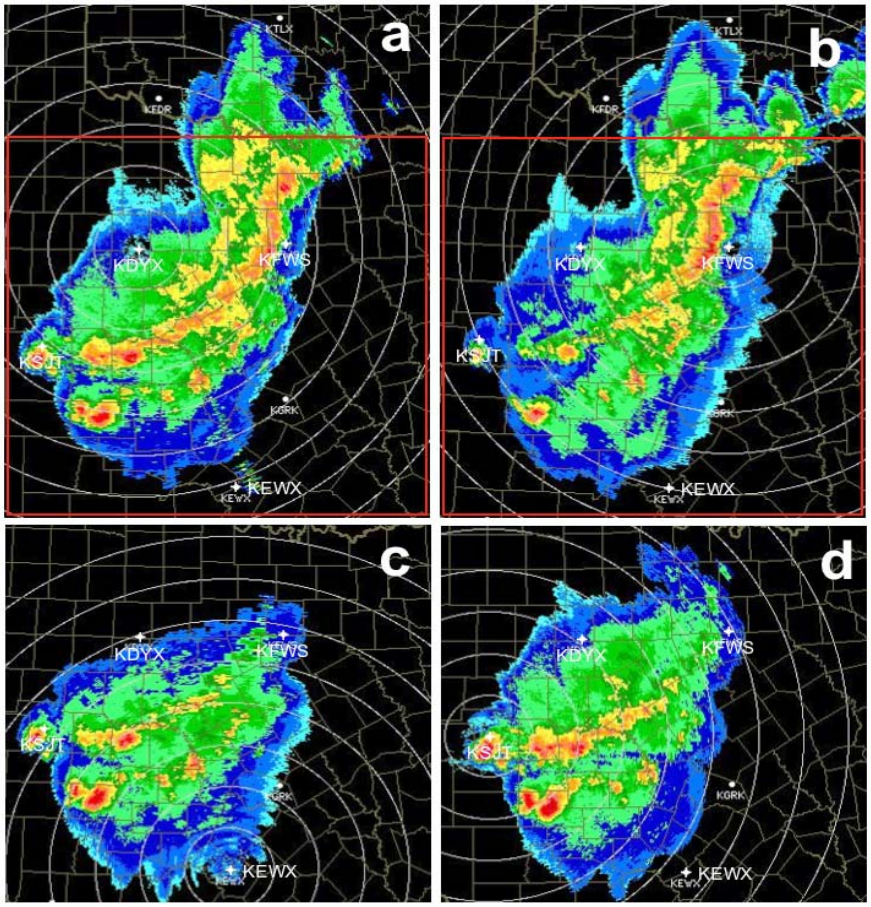

Fig. 4. Composite reflectivity fields from (a) KDYX, (b) KFWS, (c) KEWX, and (d) KSJT around 0600 UTC on June 12005. The red boxes in panels (a) and (b) indicate the common Cartesian grid for all four radars.

$$\eta_x = \frac{1}{N}\sum_{i=1}^{N} x_i \ , \tag{2a}$$

$$\eta_x = \frac{1}{N}\sum_{i=1}^{N} y_i \ . \tag{2b}$$

(3) The analysis grids from the three testing radars (KFWS, KEWX, KSJT) were advected forward in time to match the nearest validation radar (KDYX) grid. Correlation coefficients were calculated for each pair of the testing and validation fields. Table 3 provides a list of all the experiments and the results are presented in the next section.

3.3 *Results*

Figure 5 shows the correlation coefficients between the validation composite reflectivity field and the testing grid composite reflectivity field with and without synchronization towards the time of the validation field. Note that the correlation coefficients were for regions where both the validation and the test composite reflectivities were greater or equal to 30 dBZ. All of the KFWS experiments and the majority of the KEWX experiments show that there is better correlation between the validation fields and the synchronized fields than with the un-synchronized field (Figs. 5a and 5b). For the KSJT experiments, however, the un-synchronized field was better correlated with the validation field than the synchronized field (Fig. 5c). One possible cause may be that the KSJT clock is incorrect and perhaps too fast and requires further investigation. Another important factor that affects the correlation coefficients is the sampling characteristic of each radar when it observes the storms. For instance, KFWS and KDYX were close to the northern part of the squall line and captured the convective rain band very well in the reflectivity observations (Figs. 4a and 4b). The correlation coefficients showed very good consistency between the two radars composite reflectivity fields, especially when they were synchronized

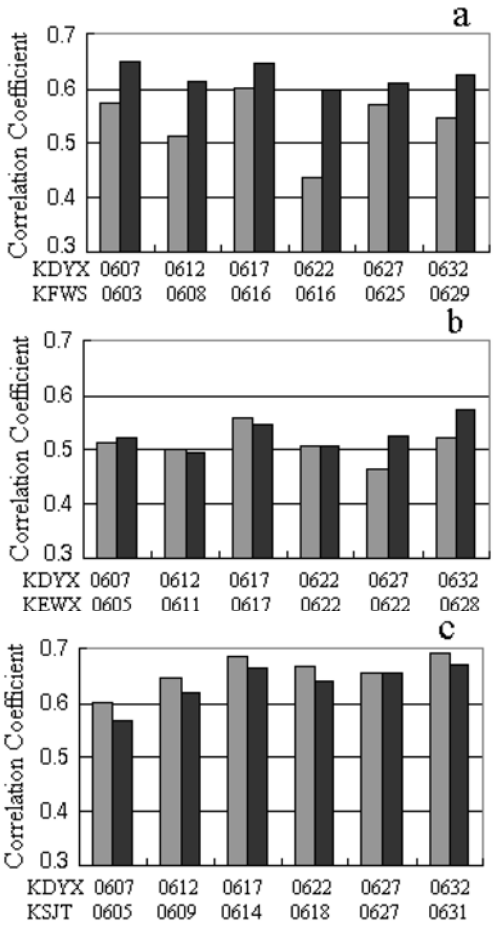

Fig. 5. Correlation coefficients between the validation composite reflectivity field of KDYX and the testing composite reflectivity of (a) KFWS, (b) KEWX and (c) KSJT with synchronization (black bar) and without synchronization (gray bar).

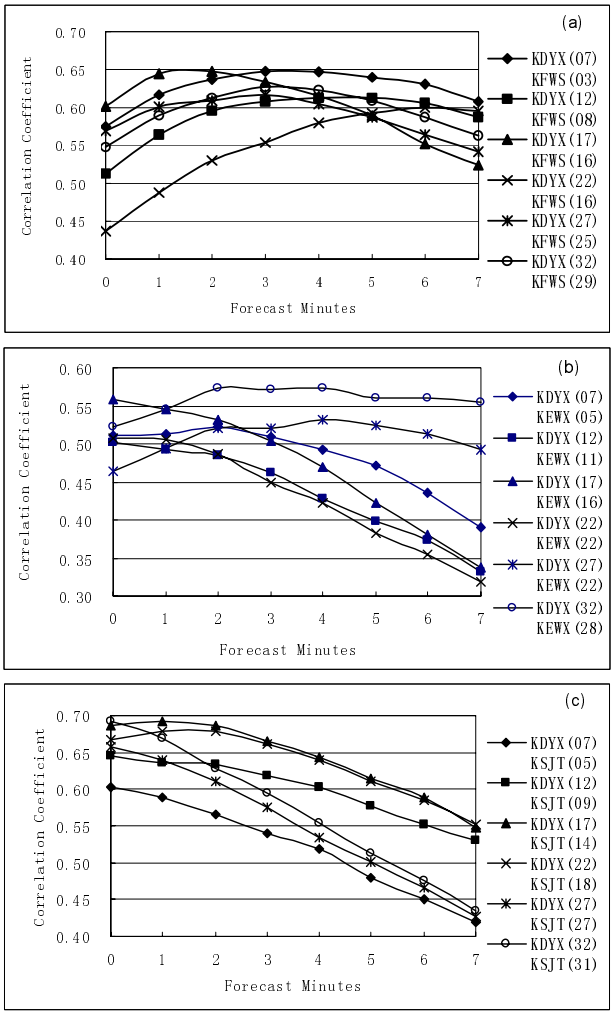

Fig. 6. Correlation coefficients between the composite reflectivity fields from KDYX observations (used as validation) and the extrapolated (in time) composite reflectivity fields from (a) KFWS, (b) KEWX, and (c) KSJT. The correlation coefficients were calculated in regions where the KDYX composite reflectivity is greater than 30 dBZ. Detailed descriptions of experiments can be found in the text.

(Fig. 5a). For the KEWX radar, however, a large part of the convective rain bands were missing in the reflectivity observations (Fig. 4c), resulting in poor correlation coefficients between the KEWX and the KDYX composite reflectivities, even with the synchronization between them (Fig. 5b). KSJT radar observations, on the other hand, captured the squall line rain band better than the KEWX radar (Fig. 4d), which resulted in better correlation coefficients with the KDYX data (Fig. 5c).

A series of forecast experiments were carried out in association with those listed in Table 3. In each experiment, the testing grid was advected forward in time at 1 minute intervals for up to 7 minutes. There were 7 forecasts for each experiment and the forecast lengths were 1, 2, 3, 4, 5, 6, 7 min, respectively. For instance, in the experiment "KDYX(07)KFWS(03)", the composite reflectivity from KFWS valid at 0603 UTC on 1 June 2005 was extrapolated to 0604, 0605, 0606, 0607, 0608, 0609, 0610 UTC, respectively. Each of the 7 extrapolated composite reflectivity fields was then compared to a validation composite reflectivity field from KDYX valid at 0607 UTC and correlation coefficients were obtained (diamond line in Fig. 6a). Note that the correlation coefficients were computed for various reflectivity thresholds.

Most correlation coefficients for the KFWS and KEWX radar experiments reached a maximum when the forecast time was near the validation time. For instance, experiments "KDYX(07)KFWS(03)" (diamond marked line in Fig. 6a) and "KDYX(12)KFWS (08)" (square line in Fig. 6a) both have the max-

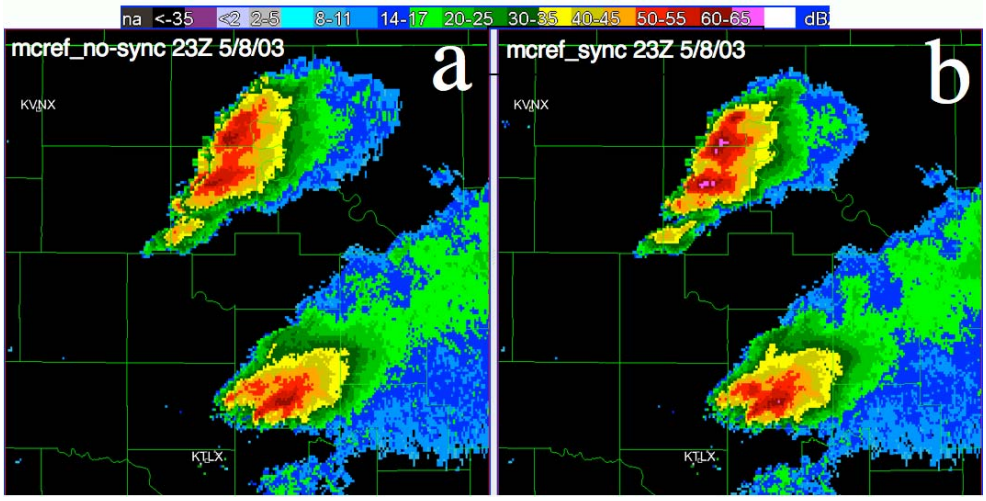

Fig. 7. Composite reflectivity mosaic using observations from KVNX and KTLX radar (a) without and (b) with the synchronization. The data was valid at 2300 UTC on 8 May 2003.

imum correlation coefficients around 4 min. Experiment "KDYX(07)KFWS(05)" (diamond line in Fig. 6b) has a maximum correlation coefficient at 2 min and experiment "KDYX(32)KEWX(28)" has a maximum at 4 min. This indicates that the vector fields used for extrapolation were representative of the storm movements. In addition, the clocks of the two radars are well synchronized, but the maximum of correlation coefficients for the KSJT experiments were not consistent with the validation data time (Fig. 6c). The precision of radar clocks is assured in the WSR-88D radar network by the implementation of the Open Radar Data Acquisition (ORDA, Istok et al., 2002). The ORDA clocks automatically synchronize to the Atomic Clock and assure that the base data time stamps are always correct. Therefore, the present technique still has practical usefulness for the WSR-88Ds or any other radar networks that include similar accurate clock calibrations. The radar data used in this study, however, were collected before the implementation of the ORDA, thus potential time clock errors were still possible (e.g., the KSJT time clock may out of calibration).

4. Summary

The current study quantitatively evaluated a multi-scale storm tracking algorithm and its application in the synchronization of radar data. The accuracy of the storm-tracking algorithm was first evaluated using a typhoon and a tornadic supercell event. It was found that the forecasts based on the storm-tracking scheme was poorer than the persistence forecast for slow moving precipitation systems because the errors in the tracking procedure overweigh the differences in reflectivity observations due to time differences. For fast moving storms, the forecasts based on storm-tracking showed better performance than persistence because of the large differences in the reflectivity fields at different times. Figure 7 shows an example of a composite reflectivity mosaic using data from two radars with and without the synchronization. The composite reflectivity with the synchronization (Fig. 7b) showed stronger storm cores than that without (Fig. 7a) because storm cores observed by the two radars were better aligned after the synchronization. Detailed synchronization experiments were then carried out for a squall line event using several radars that were closely located. The results showed that reflectivity fields from different radars correlated better when they are synchronized than when they are not. These results indicate that the synchronization of radar observations can potentially provide improved depictions of storm structure in multi-radar mosaic analyses and can have positive impacts on severe storm applications.

Acknowledgements. Major funding for this research was provided under the United States Federal Aviation Administration (FAA) Aviation Weather Research Program Advanced Weather Radar Technologies Product Development Team Memorandum Of Understanding (MOU) and partial funding was provided under NOAA-University of Oklahoma Cooperative Agreement Grant No. NA17RJ1227, U.S. Department of Commerce. Mr. Shunxin Wang contributed to the initial development of the WSR-88D's volume scan data process code. The authors are thankful to Prof. Peiyuan Zhang for his review

and discussions that helped the manuscripts greatly.

REFERENCES

Anagnostou, E. N., and W. F. Krajewski, 1999: Real-time radar rainfall estimation. Part I: Algorithm formulation. *J. Atmos. Oceanic Technol.*, **16**, 189–197.

Brewster, K., 2003: Phase-correcting data assimilation and application to storm-scale numerical weather prediction. Part I: Method description and simulation testing. *Mon. Wea. Rev.*, **131**, 480–492.

Fulton, R. A., J. P. Breidenbach, D. J. Seo, D. A. Miller, and T. O'Bannon, 1998: The WSR-88D rainfall algorithm. *Wea. Forecasting*, **13**, 377–395.

Gao, J., M. Xue, K. Brewster, and K. Droegemeier, 2004: A three-dimensional variational data analysis method with recursive filter for doppler radars. *J. Atmos. Oceanic Technol.*, **21**, 457–469.

Golding, W., 1998: Nimrod: A system for generating automated very short range forecasts. *Meteor. Appl.*, **5**, 1–16.

Hu, M., M. Xue, and Keith Brewster, 2006: 3DVAR and cloud analysis with WSR-88D Level-II data for the prediction of the Fort Worth, Texas, tornadic thunderstorms. Part I: Cloud analysis and its impact. *Mon. Wea. Rev.*, **134**, 675–698.

Istok, M., A. Zahrai, R. Saffle, R. Rivera, D. Martindale, and R. Khanna, 2002: Near term planned mission enhancements for the WSR-88D open radar data acquisition system. Preprints, *18th Conference on Interactive Information and Processing Systems*, 5.12, Amer. Meteor. Soc., 14–17 Jan., Orlando, Fla..

Johnson, J. T., P. L. MacKeen, A. Witt, E. D. Mitchell, G. J. Stumpf, M. D. Eilts, and K. W. Thomas, 1998: The storm cell identification and tracking algorithm: An enhanced WSR-88D algorithm. *Wea. Forecasting*, **13**, 263–276.

Lakshmanan, V., 2003: Motion estimator based on hierarchical clusters. *19th IIPS Conference*, Amer. Meteo. Soc., Long Beach, CA.

Lakshmanan, V., R. Rabin, and V. DeBrunner, 2003: Multiscale storm identification and forecast. *Atmospheric Research*, **67**, 367–380.

Lakshmanan, V., T. Smith, K. Hondl, G. J. Stumpf, and A. Witt, 2006: A real-time, three dimensional, rapidly updating, heterogeneous radar merger technique for reflectivity, velocity and derived products. *Wea. Forecasting*, **21**, 802–823.

Langston, C., J. Zhang, and K. Howard, 2007: Fourdimensional dynamic radar mosaic. *J. Atmos. Oceanic Technol.*, **24**, 776–790.

Liu, H., V. Chandrasekar, and G. Xu，2001: An adaptive neural network scheme for radar rainfall estimation from WSR-88D observations. *J. Appl. Meteor.*, **40**, 2038–2050.

Mitchell, E. D., S. V. Vasiloff, G. J. Stumpf, A. Witt, M. D. Eilts, J. T. Johnson, and K. W. Thomas. 1998: The National Severe Storms Laboratory Tornado Detection Algorithm. *Wea. Forecasting*, **13**, 352–366.

Seo, D. J., C. R. Kondragunta, K. Howard, S. V. Vasiloff, and J. Zhang, 2005: The national mosaic and multisensor QPE (NMQ) project-status and plans for a community testbed for high-resolution multisensor quantitative precipitation estimation (QPE) over the United States. Preprints, *19th Conf. on Hydrology*, Amer. Meteor. Soc., 10–13 Jan. 2005, San Diego, CA, CD-ROM.

Sheng, C. Y., Y. F. Pu, and S. T. Gao, 2006: Effect of Chinese doppler radar data on nowcasting output of mesoscale model. *Chinese J. Atmos. Sci.*, **30**(1), 93–107. (in Chinese)

Smith, T. M., K. L. Elmore, and S. A. Dulin, 2004: A damaging downburst prediction and detection algorithm for the WSR-88D. *Wea. Forecasting*, **19**, 240–250.

Sun, J., and N. A. Crook, 1998: Dynamical and microphysical retrieval from doppler radar observations using a cloud model and its adjoint. Part II: Retrieval experiments of an observed florida convective storm. *J. Atmos. Sci.*, **55**, 835–852.

Witt, A., M. D. Eilts, G. J. Stumpf, J. T. Johnson, E. D. Mitchell, and K. W. Thomas, 1998: An enhanced hail detection algorithm for the WSR-88D. *Wea. Forecasting*, **13**, 286–303.

Zhang, J., K. Howard, and J.J. Gourley, 2005: Constructing three-dimensional multiple radar reflectivity mosaics: Examples of convective storms and stratiform rain echoes. *J. Atmos. Oceanic Technol.*, **22**, 30–42.

Zhang, J., K. Howard, W. Xia, C. Langston, S. Wang, and Y. Qin, 2004: Three-dimensional high-resolution national radar mosaic. Preprints, *The 11th Conference on Aviation, Range, and Aerospace Meteorology*, Amer. Meteor. Soc., 4–8 October 2004, Hyannis, MA. CD-ROM.

Zhang, J., 1999: Moisture and diabatic initialization based on radar and satellite observations. Ph. D. dissertation, University of Oklahoma，203pp.